Special Issue on Control Theory Applied in Renewable Energy

Non-linear control of the output stage of a solar micro-inverter

This paper presents a proposal to control the output stage of a solar micro-inverter to inject real power into the grid. The input stage of the microinverter is enforced to extract the maximum available power of a photovoltaic module and transmit it to the inverter with an admissible voltage level. The output stage of the microinverter is studied as a grid-connected Power Source Inverter (PSI) which guarantees a high power quality level. The proposed control is composed of a sinusoidal current reference generator and a tracking system. The reference is obtained by a Phase Locked Loop (PLL) giving the shape, the frequency and phase of the current signal whose amplitude is obtained from a control loop regulating the DC voltage at the input of the inverter. The tracking of the current reference is accomplished by means of a first order sliding-mode control law allowing a simple and reliable solution. The overall control problem is theoretically solved and the theory is validated using simulation and experimental results.

Keywords: sliding-mode control; photovoltaic microinverter; power source inverter; power electronics; current controller; power quality

1. Introduction

The application of the control theory in the field of power electronics has allowed an important development of the electronic equipment to integrate the renewable resources such as solar, wind and others in the power systems (Philipson, 2010; Blaabjerg, Chen & Kjaer, 2004; Carrasco et al., 2006; Eltawil & Zhao, 2010). Normally, those apparatus are power converters which are composed by either a grid-connected inverter in the case of single stage topologies, or a DC-DC converter and a grid-connected inverter in a double stage topology, or any configuration of more than two converters having always at least a grid-connected inverter in the output stage (Xue, Chang, Kjaer, Bordonau & Shimizu, 2004; Schimpf & Norum, 2008; Kjaer, Pedersen & Blaabjerg, 2005; Calais, Myrzik, Spoone & Agelidis, 2005). The selection of the more appropriate topology depends on the power level and the number of photovoltaic (PV) modules feeding the converter. In this sense, it can be noted a trend to the development of low-power generators (less than 250 W) using a few PV modules which have been named as micro-inverters or module integrated converters (Sher & Addoweesh, 2012; Zhou, Liu & Li 2013; Edwin, Weidong & Khadkikar, 2014; Amirahmadi, Chen, Somani, Hu, Kutkut & Bartarseh, 2014). In that group of converters, the double stage topology is recognized as the more advantageous considering the possibility to separate the control functions obtaining an improved performance (Kjaer, Pedersen & Blaabjerg, 2012; Cruz Martins & Demonti, 2002). Then, the input stage (DC-DC converter) guarantees the extraction of the maximum power of the PV module whereas the output stage (DC-AC converter) ensures the injection of that power into the grid. Besides, the use of two conversion stages allows considering transformer-less topologies which avoid the use of a transformer boosting the low voltage levels of the PV modules (Zhou, Liu & Li, 2013; Meneses, Blaabjerg, García & Cobos, 2013; Kerekes, Teodorescu, Rodriguez, Vazquez & Aldabas, 2011; Calais, Agelidis & Dymond, 2011; Xiao, Xie, Chen & Huang, 2011; Yu, Lai, Qian & Hutchens, 2011; Vasconcelos Araújo, Zacharias & Mallwitz, 2010; Beser, Arifoglu, Camur & Beser, 2010). However, it is worth to recognize that the transformer- based solutions can show even higher efficiencies due to the reduced number of components (Sukesh,

Pahlevaninezhad & Jain, 2014; Kim, Jan, Shin & Won, 2014; Gao, Chen, Zhang & Qian, 2014; Zhang, He & Liu, 2013; Edwin, Weidong & Khadkikar, 2014; Kim, Shin, Lee, Jung & Won, 2014).

The use of a transformer-less double stage topology implies the existence of a DC-Link or a pseudo DC-Link as it is described and studied in (Li & Wolfs, 2008). The use of a DC-link allows having a better decoupling of the power grid to the PV module and also allows improving many characteristics of the power device. For instance, the use of higher voltages in the DC link allows using lower capacitances easily achievable with thin film capacitors, this considerably increasing the life- time and the efficiency of the converter. Additionally, the natural oscillations produced at the DC side of the output stage of the microinverter are supported in the DC-link but not in the PV module, which increases its life- time. Then, the study of the dual-stage microinverters is motivated by the required understanding of the whole system in order to reduce the impact of the additional complexity and to reveal all possible potentialities.

The connection of a full bridge converter to the grid through a series inductor allows obtaining a desired waveform in the output current which facilitates the control of the power interaction with the grid. The full bridge inverter works with an energy source always available at the DC side which corresponds to the DC link in the case of the double stage microinverter. Depending on the nature of that source, the inverter can be classified as a Voltage Source Inverter (VSI) or a Current Source Inverter (CSI) (Rashid, 2001). However, considering that the input stage of the microinverter is enforced to have a power source nature, the inverter can be studied as a Power Source Inverter (PSI). That behavior is obtained using a control law in the DC-DC converter to have impedance matching with the PV module, ensuring at the same time the availability of the extracted power in the DC-link. This behavior can be obtained using a sliding-mode based control to enforce a Loss-Free-Resistor behavior (SM-LFR) in the DC-DC converter (Cid-Pastor, Martinez-Salamero, El Aroudi, Giral, Calvente & Leyva 2013; Singer, 1990). The discussion in this paper is delimited to the DC-AC stage of the microinverter and then it is assumed the existence of a power source at the DC-link.

The control of the DC-AC stage requires the generation of a proper current reference and a way to robustly track it. To generate this reference it is necessary to obtain the frequency and phase of the grid voltage which can be extracted either directly using the grid voltage signal or indirectly using a synchronization system. Among these two possibilities, the more relevant difference is that in the direct way approach, the harmonic content of the voltage is transferred to the current increasing the levels of the Total Harmonic Distortion (THD), which prevents the compliance of the related standards in terms of the power quality (IEC Standard, 1995; IEEE Standard, 2005; UL Standard, 2010; IEEE Standard, 2000; IEC Standard, 2002). Then, obtaining the frequency and phase from a Phase Looked Loop (PLL) can result in a synchronized sinusoidal signal with a very low THD. The amplitude of that reference can be determined by a control loop ensuring the power balance of the overall system. Then, using a dual stage topology, the control of the inverter can be used to regulate the voltage of the DC-link modifying the power injected into the grid through the amplitude of the inductor current (Zhang, Sun, Xing, Feng & Ge, 2011; Karimi-Ghartemani, Khajehoddin, Jain & Bakhshai, 2013).

In order to obtain the tracking of the current reference, many control methods have been applied. The simplest one consists in using a comparator operating at constant frequency (Rodriguez & Amaratunga, 2006). Other method which implies a lower complexity is the hysteresis control which can be applied using either a constant hysteresis band or an adaptive hysteresis band (Krismadinata, Rahim & Selvaraj, 2007; Dai & Chao, 2009; Ho, Cheung & Chung, 2009). Like in other references on tracking

applications, the predictive control is also an interesting option when digital implementation is possible (Jiang, Cao, Li & Peng, 2012; Kojabadi, Yu, Gadoura, Chang & Ghribi, 2006). Besides the mentioned strategies, the sliding mode control has been also used in grid-connected applications due to its well-known robustness, stability and simple implementation (Jiabing, Zhu, Nian, Shang & He, 2010; Fernao Pires, Sousa & Martins, 2014; Kim, 2006). Sliding mode control strategies for grid-tied inverters have been also implemented using digital devices retaining its main advantages (Negroni, Meza, Biel & Guinjoan, 2005).

This paper introduces the full bridge inverter working as a Power Source Inverter (PSI) using sliding-mode control to ensure a flawless tracking of the sinusoidal current reference. A first order sliding surface is employed to control the output current of the inverter which is studied using the equivalent control method (Utkin, Guldner & Shi, 2009; Sira-Ramirez & Silva-Ortigoza). The resulting sliding motion is used to derive a model relating the DC-link voltage and the amplitude of the output current. This model is used to design a two loop controller with a current controller as the inner loop and a voltage regulator in the outer one. The voltage regulator defines the instantaneous amplitude of the output current while the sinusoidal waveform synchronized with the grid is given by a PLL. The relation between the Total Harmonic Distortion (THD) and the Power Factor (PF) with the voltage of the DC-link is modelled and analyzed through the harmonic balance method. A compensator is proposed to have a simple but effective reduction of the oscillations in the outer control loop reducing the harmonics in the current. The theoretical analysis is verified by means of simulation and experimental results.

2. Fundamentals of grid-connected generation

Since the lower harmonic distortion of the grid voltage is normally below of 3%, the grid can be ideally considered as a pure sine-wave AC voltage source of the form

$$v_g = V_{max} \sin \omega t \tag{1}$$

where $\omega = 2\pi f$, and f is the fundamental frequency. The output current of the power generator is defined as

$$i_g = I_{max} \sin(\omega t + \varphi) \tag{2}$$

where I_{max} is a constant value defining the amplitude of the current and φ is the displacement angle with respect to the voltage. At unitary power factor φ is near zero and the amplitude of the current defines the amount of the power injected into the grid. Then, the real power is given by

$$P = P_g = \frac{I_{max} V_{max}}{2} = I_g \cdot V_g \tag{3}$$

where I_g and V_g are the RMS values of the grid voltage and current respectively. However, depending on the control performance, the current injected may be more or less distorted with more or less phase-shift with respect to the mains voltage. In these cases, the above definition of the grid current can be generalized as

$$i_g = I_1 \sin(\omega t + \varphi) + \sum_{k=2}^{n} I_n \sin(n\omega t + \varphi_n) \tag{4}$$

The current THD-R (relative to the RMS value) is computed as follows:

$$THD - R = \frac{I_h}{I_g} = \sqrt{1 - \left(\frac{I_1}{I_g}\right)^2} \tag{5}$$

where I_h is the RMS value of the harmonic content in the current I_g and the power factor (PF) is defined by:

$$PF = \frac{P}{S} = \frac{I_1 \cos(\varphi)}{I_g} \tag{6}$$

Therefore, the DC-AC stage converts the power available in the DC-link and injects it into the grid. This has to be done ensuring a high power quality level in the grid connection, or in other words a unitary PF along with a lower current THD. These two problems are the main challenges for the control of a grid-connected inverter.

Due to the adopted control strategy, the amplitude of the current injected to the grid is not constant, this introducing some differences with respect to the expected ideal behavior. Therefore the current of the inverter will be forced to follow a current reference given by $i_{g_{ref}}(t) = i_{max}(t) \sin \omega t$.

3. Converter model

Two different commutation modes can be applied in the full bridge inverter: the bipolar commutation and the unipolar commutation. The model of the converter operating in each mode can be obtained from a combination of the different possible circuit configurations depicted in table 1 using the rows a, b, c and d to show the corresponding equations and switch conditions. On the one hand, using bipolar or two-level commutation, the switches of each leg operate complementarily, in such a way that, the high-side switch is off when the low-side switch is on , and the high-side switch is on when the low-side switch is off. Further, each leg operates complementarily with respect to the other one. Then, the circuit configuration changes among the circuit structures in the rows **a** and **c** of table 1. In this mode the inverter can track a current reference with relative simplicity. However, the switching losses are higher because both legs commute at high frequency. Further, it is worth to mention that some studies show that in photovoltaic systems the ground current is lower when the inverter uses bipolar commutation (Baker, Agelidis & Nayer, 1997).

On the other hand, the unipolar operation of the full bridge can be obtained forcing a leg to switch at high frequency while the other one switches at grid frequency. Also, it is possible to switch the high side switches of both legs at high frequency while the low side switches commute at grid frequency (National Semiconductors, 2011). Each pair of switches operating at the same frequency commutates complementarily. Using this commutation mode, four circuit structures are possible, two for the positive half-cycle (rows **a** and **b** in table 1), and two for the negative half-cycle (rows **c** and **d** in table 1). Thus, as a consequence of the commutation, the switching losses are reduced because only two switches operate at high frequency.

Table 1. Circuit structures for the H-bridge inverter

	Circuit configuration and power flow	Expressions
a	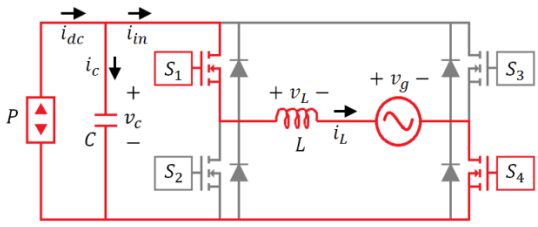	**S_1, S_4 are on** **S_2, S_3 are off** $v_L = v_C - v_g$ $i_C = i_{dc} - i_{in}$ $i_{in} = i_L$
b	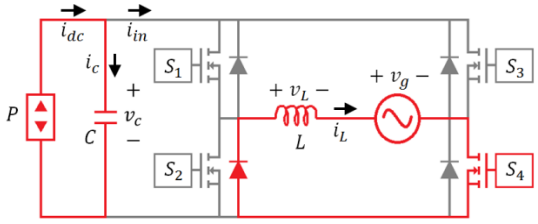	**S_2, S_4 are on** **S_1, S_3 are off** $v_L = -v_g$ $i_C = i_{dc}$
c	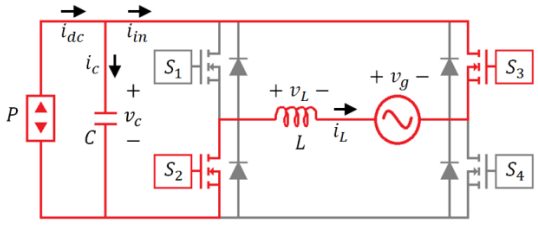	**S_1, S_4 are off** **S_2, S_3 are on** $v_L = -v_C - v_g$ $i_C = i_{dc} - i_{in}$ $i_{in} = -i_L$
d	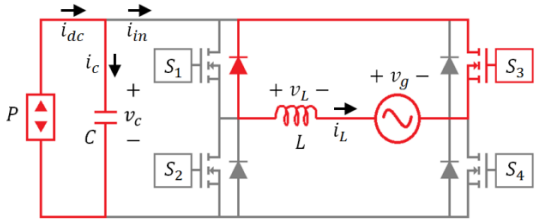	**S_2, S_4 are OFF** **S_1, S_3 are ON** $v_L = -v_g$ $i_C = i_{dc}$

2.1. Model using bipolar commutation

By defining the control variable u such that $u = 1$ when S_1 and S_4 are on, and $u = -1$ when S_2 and S_3 are on, the following equations are obtained

$$L\frac{di_L}{dt} = -v_g + v_C u \tag{7}$$

$$C\frac{dv_C}{dt} = i_{dc} - i_L u = \frac{P}{v_c} - i_L u \tag{8}$$

2.2. Model using unipolar commutation

Using the same variable u as in the bipolar case for the positive half-cycle of the grid voltage (rows **a** and **b** in table 1), the following equations are derived

$$L\frac{di_L}{dt} = -v_g + v_C u \tag{9}$$

$$C\frac{dv_C}{dt} = i_{dc} - i_L u_1 = \frac{P}{v_c} - i_L u \tag{10}$$

The operation in the negative half-cycle is similar but the inductor current flows in the opposite direction (rows **c** and **d** in table 1). The corresponding equations are given by

$$L\frac{di_L}{dt} = -v_g - v_C(1-u) \tag{11}$$

$$C\frac{dv_C}{dt} = i_{dc} - i_L u = \frac{P}{v_c} + i_L(1-u) \tag{12}$$

Then, it is possible to write equations (9), (10), (11) and (12) in the compact form given below

$$L\frac{di_L}{dt} = -v_g + v_C u - \frac{v_C}{2}\left(1 - \text{sign}(v_g)\right) \tag{13}$$

$$C\frac{dv_C}{dt} = \frac{P}{v_c} - i_L u + \frac{i_L}{2}\left(1 - \text{sign}(v_g)\right) \tag{14}$$

4. Sliding-mode current control

Both types of commutation can be used in the full-bridge inverter to track a current reference injecting real power into the grid. The use of the sliding mode control consists in defining a sliding surface using a sinusoidal current reference for the output current of the inverter. A fundamental condition ensuring the efficiency of this strategy is that the dynamic behavior of the current reference is significantly slower than the current dynamics of the inductor that couples the inverter to the grid. This fact imposes a switching frequency for the converter much higher than the frequency of the grid. Under these conditions, the output current of the inverter is constrained to be in a neighborhood of the current reference, obtaining the expected power injection. To prevent the problems associated with a very high switching frequency, a hysteresis band is introduced limiting the current variation around the current reference in the way illustrated in figure 1.

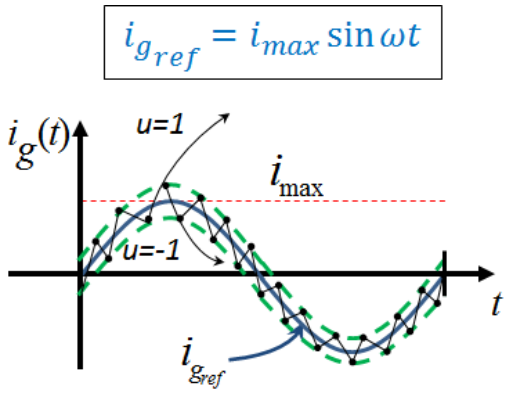

Figure 1. H-bridge grid-connected PSI.

The full bridge inverter is coupled to the grid through a single inductor and decoupled to the DC-link through a simple capacitor, so that it is a second order system. Applying the equivalent control method to analyze the sliding motion, a reduced model of the converter dynamics is obtained. This model describes the dynamics of the system for a current reference imposed by the sliding surface. However, considering that some harmonics can appear in the reference as a consequence of the presence of harmonics in the amplitude value given by the control, the amplitude of the reference is considered constant and then it is defined by the time-varying signal i_{max}.

4.1. Bipolar commutation

Defining the first order sliding surface

$$S(x) = i_{g_{ref}} - i_L = i_{max} \sin \omega t - i_L \tag{15}$$

the current loop enforces that $i_L = i_{g_{ref}}$, and hence $i_g = i_{max} \sin \omega t$. The sliding motion is achieved using the control law:

$$u = \begin{cases} 1 & when\ \ S(x) > 0 \\ -1 & when\ \ S(x) < 0 \end{cases} \tag{16}$$

Applying the invariance conditions $\left(S(x) = 0, \dot{S}(x)\big|_{u=u_{eq}} = 0\right)$ leads to:

$$\frac{dS(x)}{dt} = \frac{i_{g_{ref}}}{dt} - \frac{di_L}{dt} = \frac{di_{max}}{dt} \sin \omega t + \omega i_{max} \cos \omega t + \frac{v_g}{L} - \frac{v_C u}{L} = 0 \tag{17}$$

The equivalent control is deduced as

$$u_{eq} = \frac{1}{v_C}\left(L \frac{di_{max}}{dt} \sin \omega t + \omega L i_{max} \cos \omega t + V_{max} \sin \omega t\right) \tag{18}$$

which is constrained in the interval $-1 < u_{eq} < 1$. Replacing the equivalent control (18) in (10), the following resulting sliding dynamics is obtained.

$$C \frac{dv_C}{dt} = \frac{P}{v_C} - \frac{i_{max} \sin \omega t}{v_C}\left(L \frac{di_{max}}{dt} \sin \omega t + \omega L i_{max} \cos \omega t + V_{max} \sin \omega t\right) \tag{19}$$

When i_{max} is constant and equal to I_{max}, the reachability of the sliding surface can be obtained analyzing the condition $S(x)\, \dot{S}(x) < 0$, which leads to

$$v_C(t) > \sqrt{L^2 \omega^2 {I_{max}}^2 + {V_{max}}^2} \sin\left(\omega t + \operatorname{atan}\left[\frac{\omega L I_{max}}{V_{max}}\right]\right) \tag{20}$$

4.2. Unipolar commutation

Defining the previous first order sliding surface $S(x) = i_{g_{ref}} - i_L$, the equality $i_L = i_{g_{ref}}$ is enforced. The sliding motion is achieved using the same control law (16). Now, the invariance conditions $\left(S(x) = 0, \dot{S}(x)\big|_{u=u_{eq}} = 0\right)$, lead to $\frac{dS(x)}{dt} = \frac{di_{g_{ref}}}{dt} - \frac{di_L}{dt}$, from which:

$$\frac{dS(x)}{dt} = \frac{di_{max}}{dt} \sin \omega t + \omega i_{max} \cos \omega t + \frac{v_g}{L} - \frac{v_C}{L} u + \frac{v_C}{2L}\left(1 - \operatorname{sign}(v_g)\right) \tag{21}$$

The equivalent control can is given by

$$u_{eq} = \frac{1}{v_C}\left(L\frac{di_{max}}{dt}\sin\omega t + \omega L i_{max}\cos\omega t + V_{max}\sin\omega t + \frac{v_C}{2}\left(1 - \text{sign}(v_g)\right)\right) \quad (22)$$

This equivalent control is then constrained to be in the interval $-1 < u_{eq} < 1$. Replacing the equivalent control (22) into (14), the following resulting sliding dynamics is obtained

$$C\frac{dv_C}{dt} = \frac{P}{v_C} - \frac{i_{max}\sin\omega t}{v_C}\left(L\frac{di_{max}}{dt}\sin\omega t + \omega L i_{max}\cos\omega t + V_{max}\sin\omega t\right) \quad (23)$$

When i_{max} is constant and equal to I_{max}, the reachability conditions of the sliding surface are deduced from $S(x)\,\dot{S}(x) < 0$ leading to the condition

$$v_C(t) > \sqrt{L^2\omega^2 {I_{max}}^2 + {V_{max}}^2}\,\sin\left(\omega t + \text{atan}\left[\frac{\omega L I_{max}}{V_{max}}\right]\right) \text{ and}$$
$$2k\pi - \text{atan}\left|\frac{I_{max}L\omega}{V_{max}}\right| < \omega t < (2k+1)\pi - \text{atan}\left|\frac{I_{max}L\omega}{V_{max}}\right| \quad (24)$$

5. Control of the DC-Link

An interesting way to stabilize and regulate the DC voltage consists in considering the current control as the inner loop of a cascade- type controller whose voltage outer controller modifies the amplitude of the current sinusoidal reference of the inner loop (see figure 2). In fact, the outer loop ensures that the average value of the voltage in the DC-link is permanently regulated. Thus, the power balance on the overall microinverter is guaranteed because the voltage in the storage energy element of the middle-point (DC-link) is kept around a constant value.

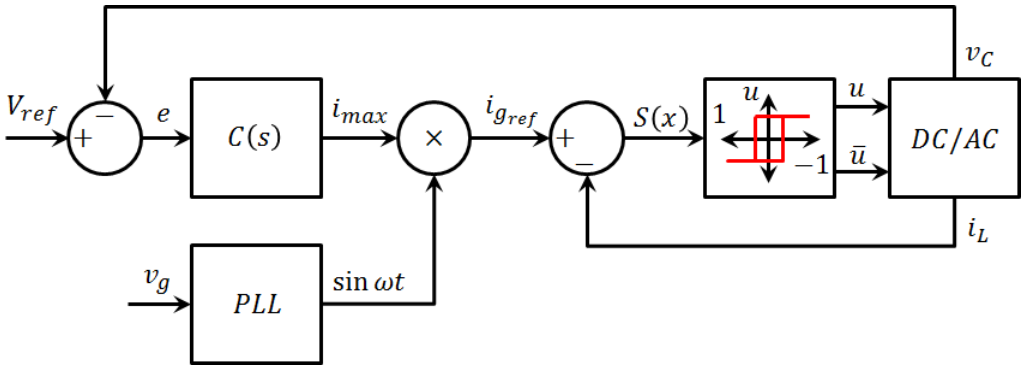

Figure 2. Block diagram of the two-loop controller for the grid-connected inverter.

Now, a dynamic model having the voltage of the DC-link as a function of the amplitude of the output current is necessary for designing appropriately the outer loop controller $C(s)$.

5.1. Model of the DC-Link voltage

Note that both types of commutation (unipolar, bipolar) lead to the same resulting sliding dynamics. Recalling that $\sin\omega t\cos\omega t = \sin 2\omega t\,/2$ and $\sin^2\omega t = (1-\cos 2\omega t)/2$, expressions (19) or (23) can be equivalently written as

$$Cv_C\frac{dv_C}{dt} = P - \frac{Li_{max}}{2}\frac{di_{max}}{dt} + \frac{Li_{max}}{2}\frac{di_{max}}{dt}\cos 2\omega t - \frac{L\omega {i_{max}}^2}{2}\sin 2\omega t - \frac{V_{max}i_{max}}{2} + \frac{V_{max}i_{max}}{2}\cos 2\omega t \tag{25}$$

Now, if $i_{max}(t)$ is not a constant but a slow variable over an interval of time of length $T = \pi/\omega$, we can suppose that $i_{max}(t)$, $\frac{di_{max}}{dt}(t)$ and P do not vary significantly. Then, integrating (25) from t to $t+T$ leads to

$$\frac{1}{T}\int_t^{t+T} Cv_C\frac{dv_C}{du}du = P - \frac{V_{max}i_{max}}{2} - \frac{Li_{max}}{2}\frac{di_{max}}{dt}$$

or after evaluating the integral:

$$\frac{1}{2}C\left[\frac{{v_c}^2(t+T) - {v_c}^2(t)}{T}\right] = P - \frac{V_{max}i_{max}}{2} - \frac{Li_{max}}{2}\frac{di_{max}}{dt} \tag{26}$$

which leads to the equilibrium point where $v_c(t+T) \cong v_c(t)$

$$\bar{P} = \frac{V_{max}I_{max}}{2} \tag{27}$$

Since $T = \frac{\pi}{\omega}$ is small, the following approximation can be considered

$$\frac{1}{2}C\left(\frac{{v_c}^2(t+T) - {v_c}^2(t)}{T}\right) \cong Cv_C\frac{dv_C}{dt}$$

and then, the model is given by

$$Cv_C\frac{dv_C}{dt} \cong P - \frac{V_{max}i_{max}}{2} - \frac{Li_{max}}{2}\frac{di_{max}}{dt} \tag{28}$$

where the last term on the right side is nonlinear. Denoting by $\hat{*}$ the linearized variables and retaining the first order terms, the linearized model around $I_{max}, V_{max}, V_{ref}, \bar{P}$ is obtained:

$$C\frac{d\hat{v}_C}{dt} = \frac{1}{V_C}\hat{P} - \frac{V_{max}}{2V_{ref}}\hat{\imath}_{max} - \frac{LI_{max}}{2V_{ref}}\frac{d\hat{\imath}_{max}}{dt} \tag{29}$$

Taking the Laplace transform of the previous expression for zero initial conditions, we have

$$V_C(s) = -\frac{LI_{max}s + V_{max}}{2CV_{ref}s}I_{max}(s) + \frac{1}{CV_{ref}s}P(s) \tag{30}$$

As it can be noted in (30), the voltage of the DC-link is affected by the amplitude of the output current and also by the input power. Since the amplitude of the current will be considered as the manipulated variable, the power will be considered as a disturbance.

By applying a simple feedback strategy, the block diagram depicted in figure 3 represents the closed loop system.

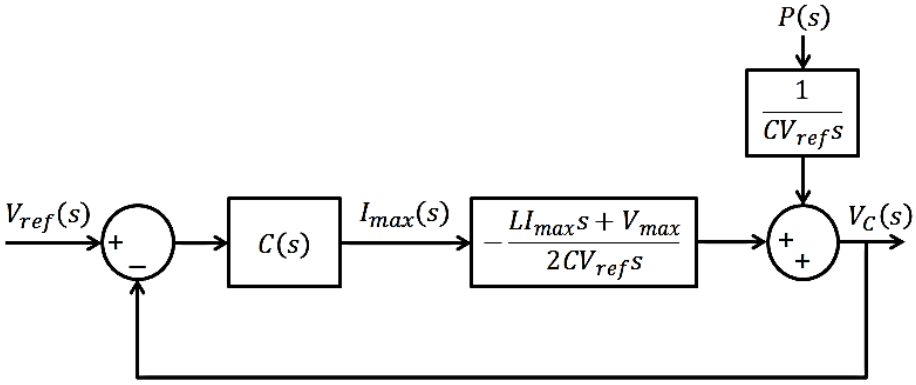

Figure 3. Block diagram of the closed-loop control system.

Note that the transfer function from $I_{max}(s)$ to $V_C(s)$ exhibits a negative sign, and it is, in fact, a simple integrator with a stable zero. Note also that integration characterizes the transfer function from power to voltage variation. Then, if it is considered that the power varies by steps, the loop will be affected by disturbances of order 2 (ramps). The controller design has to be done taking into account all these specificities.

5.2. Synthesis of a voltage loop controller

From the above discussion, since the system naturally possesses one integrator, the controller must add another one. Moreover, the controller must attenuate the effect of the DC voltage ripple in the loop signals. For this reason, a first order filter is introduced in the controller; its bandwidth will be tuned for filtering the ripple whose frequency is 2ω. Considering the previous analysis the selected controller will be given by

$$C(s) = -\frac{K_c(T_c s + 1)}{s(T_f s + 1)}, \qquad K_C, T_C, T_f > 0 \tag{31}$$

where T_f is introduced to filter the ripple of the error signal, and the negative sign compensates the sign of the converter transfer function. In addition, an analysis of the zero of the converter transfer function shows that, for the involved frequencies, it can be neglected, this leading to a simplified transfer function $G(s)$ given by

$$G(s) = \frac{V_C(s)}{I_{max}(s)} = -\frac{2CV_{ref}}{V_{max}}\frac{1}{s} = -\frac{K_{max}}{s} \tag{32}$$

For example, a value of L of 10 mH, $V_{max} = 220\sqrt{2}\ V$ and $I_{max} \leq 0.65\ A$ $(P \leq 200\ W)$ result in a zero in $s = \frac{310.2}{0.65*10} \times 10^3\ Rad/s$. From the above analysis, the controlled open loop transfer function is

$$L(s) = C(s)G(s) = \frac{K_{max}K_c(T_c s + 1)}{s^2(T_f s + 1)} \tag{33}$$

where T_f is fixed, the free parameters being K_c and T_c. They will be determined in order to have a phase margin of 45°. The first step consists in identifying the frequencies corresponding to a phase of -135° for the controlled open loop transfer function. We have

$$\text{Arg}[L(j\omega)] = -180° - \text{atan}(T_f\omega) + \text{atan}(T_c\omega) = -135° \tag{34}$$

Or, equivalently, $\text{atan}(T_c\omega) - \text{atan}(T_f\omega) = 45°$

Using the identity $\text{atan}(x) - \text{atan}(y) = \text{atan}\left(\frac{x+y}{1-xy}\right)$, then, the previous equation is expressed as

$$\text{atan}(T_c\omega) - \text{atan}(T_f\omega) = \text{atan}\left(\frac{\omega(T_c - T_f)}{1 + T_cT_f\omega^2}\right) = 45° \tag{35}$$

Then, $\frac{\omega(T_c-T_f)}{1+T_cT_f\omega^2} = 1$, which implies that $T_cT_f\omega^2 - \omega(T_c - T_f) + 1 = 0$. Since the discriminant $\Delta = {T_f}^2 - 6T_cT_f + {T_c}^2 > 0$, there exist two real roots given by

$$\omega_{1,2} = \frac{1}{2T_fT_c}\left(-T_f + T_c \pm \sqrt{{T_f}^2 - 6T_cT_f + {T_c}^2}\right) \tag{36}$$

Writing $T_c = aT_f$ with $a > 0$, the discriminant Δ will be positive if

$$a > 3 + 2\sqrt{2} > 1 \tag{37}$$

and the roots can be expressed in terms of T_f and a as

$$\omega_{1,2} = \frac{1}{2aT_f}\left((a-1) \pm \sqrt{a^2 - 6a + 1}\right) \tag{38}$$

It is easy to verify that the two roots are positive for the values of a satisfying (37). For the two frequencies $\omega_{1,2}$, the phase of the controlled open loop transfer function is equal to -135°. If the gain for $\omega_{1,2}$ is equal to 1, then the phase margin will be equal to 45°. This is true if the gain of the controller K_c is selected as

$$K_{c_{1,2}} = \frac{{\omega_{1,2}}^2}{K_{max}}\sqrt{\frac{1 + {T_f}^2{\omega_{1,2}}^2}{1 + a^2{T_f}^2{\omega_{1,2}}^2}} \tag{39}$$

Figure 4 shows the Bode plots for the two cases. As predicted by the theory, the gains $K_{c_{1,2}}$ allow fixing the phase margin at 45°. Note that a satisfying (37) constitutes a freedom degree which can be used to adjust the bandwidth of the closed loop transfer function (i.e. settling time), and observe that the phase margin has an influence on overshoots.

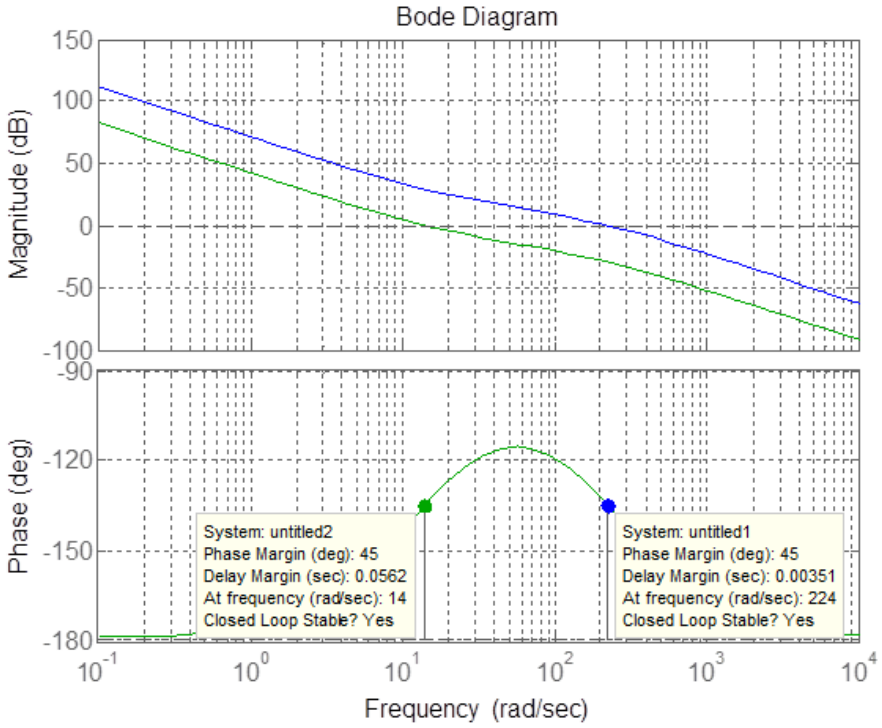

Figure 4. Bode plot showing the two possible frequencies to achieve a phase margin of 45° using the proposed controller

Finally, the design method can be summarized by the following step by step procedure:

- Select $T_f = 1/2\pi f_f$ to reject the ripple in the measurement of the DC voltage. Values of f_f around 50Hz show a good trade-off between ripple-rejection and time response performance.
- Select the value of a satisfying the condition (37). The value of a affects considerably the time response only in a range near to the constraint (37).
- Compute the value of T_c, ω_1 and consequently the controller gain $K_C = K_1$.

To design the controller using the aforementioned method, the set of parameters for the power converter and the power sources are listed in Table 2, which will be used afterwards to illustrate the theory by simulations and experimental results.

Table 2. Parameters of the converter and power sources

Parameter	Symbol	Value
Inductance	L	10 mH
DC bus Capacitor	C	22 µF
DC bus Voltage	V_C	400 V
Grid RMS Voltage	V_g	220 V
Grid Frequency	f_g	50 Hz
Power Range	P	$20 - 100$ W

For the set of parameters in table 2, the controller parameters are listed in table 3 for different values of a. The values of a are generated by a MATLAB algorithm which considers $a_k = 1 + 0.05a_{k-1}$ for values of k between 1 and 6, having $a_0 = 5.828$ satisfying (37).

Table 3. Controller parameters for $T_f = 0.004$

Parameter	$a = 5.828$	$a = 6.119$	$a = 6.731$	$a = 7.741$	$a = 9.289$	$a = 11.614$
$\omega_1(Rad/s)$	103.55	77.68	61.22	47.40	35.95	26.67
$\omega_2(Rad/s)$	103.55	131.46	151.63	170.30	187.13	201.80
$T_c(s)$	0.0233	0.0245	0.0269	0.0310	0.0372	0.0464
$K_{c_1}(\Omega^{-1}/s)$	0.5711	0.3781	0.2573	0.1656	0.1006	0.0578
$K_{c_2}(\Omega^{-1}/s)$	0.5711	0.7450	0.8224	0.8405	0.8005	0.7138

Figure 5 shows the transient responses of the closed-loop system using the results in Table 3. The responses have been generated considering a step change in the voltage reference of 20 V. It is worth pointing out that only a slight difference can be noted in the overshoot and settling time. Also, increasing the value of a does not lead to significant changes in the form of transient response.

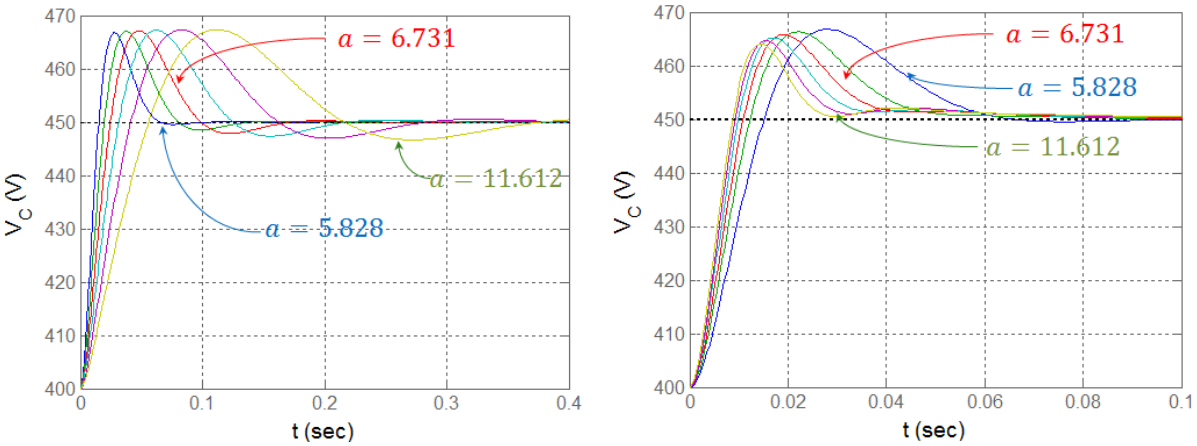

Figure 5. Responses of the closed-loop system to a step change in the reference of 50V with controllers for the values of a in table 5: a) $K_c = K_{c_1}$; and, b) $K_c = K_{c_2}$

However, as shown in figure 6, by increasing the value of a it is possible to reduce the maximum deviation of the output voltage when the converter copes with a change in the input power. In consequence, for $T_f = 0.004$, the value of $a = 11.632$ with $K_c = K_{c_2}$ allows obtaining the best response, i.e., a voltage deviation below 3.8% rejected within 0.1 s, which corresponds to five cycles at the grid-frequency approximately.

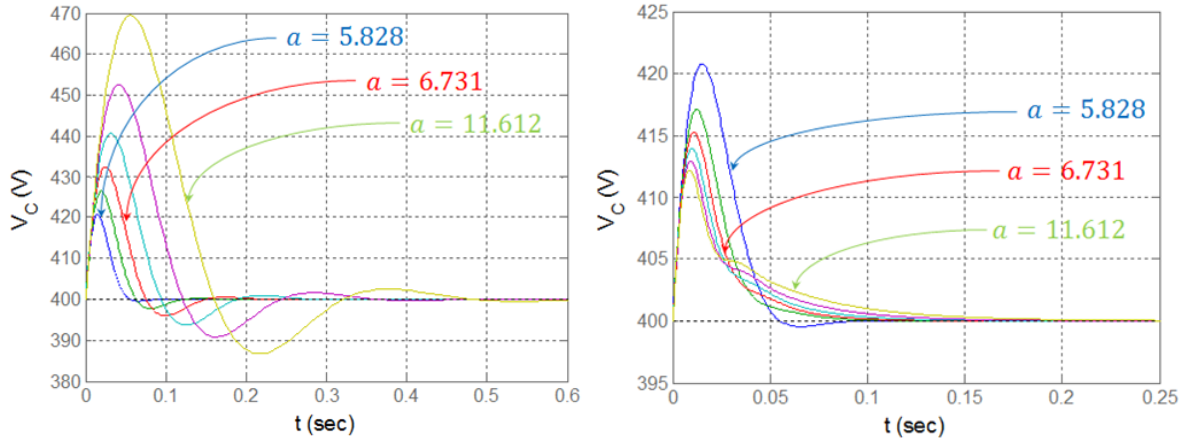

Figure 6. Disturbance rejection of the closed-loop system using the values of a in table 4.5: a) responses for $K_c = K_{c_1}$; and, b) responses for $K_c = K_{c_2}$

5.3. *Simulation results*

In order to verify the theoretical approach, several simulations have been performed in PSIM where the power source has been modelled using a voltage controlled source whose value is defined by the output current for a constant value of power. The value of the parameter T_f in the controller transfer function is selected to reject the double frequency component without enforcing a slow transient response. Considering a grid frequency of 50 Hz, then the low pass filter must reject a 100 Hz (628 Rad/s) component. If a value of 5 ms is selected for T_f, then, an attenuation of approximately -10 dB is ensured at the double grid frequency. Hence, from the analysis in the above section, a value of $a = 12$ is selected, with a value of 0.06 s for T_c. A value of 0.4477 for K_c is then computed for a frequency $\omega_2 = 162.86$ Rad/s. The resulted controller is

$$C(s) = -\frac{0.4477(0.6s + 1)}{s(0.005s + 1)} \tag{40}$$

Figure 7 shows the transient response of the system when a step is applied to the reference value. When the equilibrium point of 400 V for the DC bus voltage is attained, the reference value changes to 450 V at 0.6 s. The reference value returns to 400 V abruptly after one second. It is possible to observe that the controlled system has the desired regulation with zero error and shows a good performance in the time response.

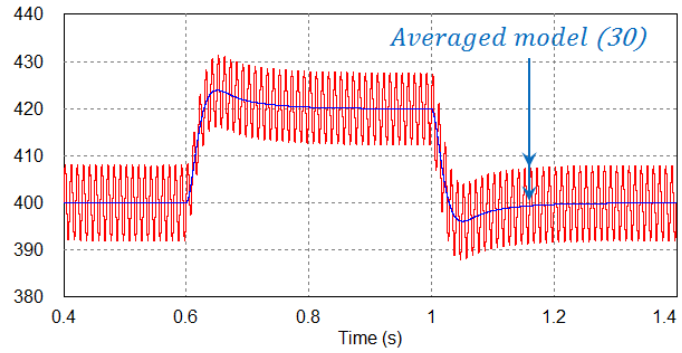

Figure 7. Simulation results to set-point changes of the DC-bus voltage reference value

Figure 8 shows the transient responses of the system when a sudden additive disturbance is applied to the input power. After reaching the equilibrium point of 400 V for an input power of 50 W, the input power changes to 100 W at 0.2 s. The power returns to 50 W after 0.5 seconds. It is possible to observe that the controlled system rejects the disturbance showing a maximum voltage deviation of 15% controlled within 0.2 s.

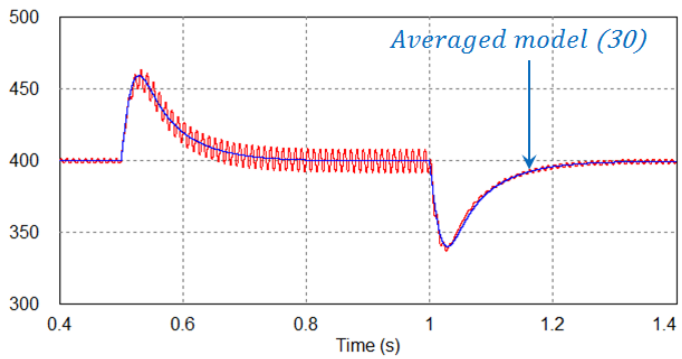

Figure 8. Simulation results of disturbance rejection for sudden changes in the input power

It is worth to note that both figures 7 and 8 show a good correspondence between the behavior of the average model and that of the switched one. At the same time, it is shown that the controller must reject the influence of the ripple of the DC bus voltage ensuring a quality level of the injected power. Figure 9 shows the waveform of the inductor current for two different powers in the operational range: 20 W and 100W. THD values lower than 5% are obtained for both cases.

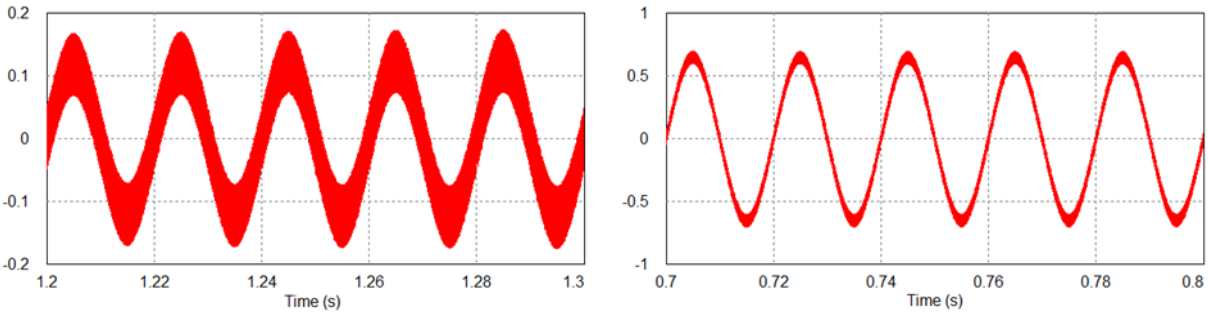

Figure 9. Current waveforms for two operational points of the grid connected inverter: a) 20 W; b) 100 W.

6. Power quality analysis

6.1. Modelling of the voltage ripple of the DC-Link

In order to have an accurate representation of the system variables and quantify the parametric dependence between them, it is possible to study the harmonic balance of the power between the DC side and the grid side. If ideal synchronization is considered, the AC side is defined by the expressions:

$$v_g(t) = V_{max}\, sin\, \omega t \tag{41}$$

$$i_g(t) = i_{max}(t)\, sin\, \omega t \tag{42}$$

Whereas the voltage of the DC side can be defined as:

$$v_C(t) = V_{dc} + V_2\, sin(2\omega t + \gamma) \tag{43}$$

Note that only an oscillatory component at the double frequency of the grid has been introduced and also note that this component has a phase displacement γ with respect to the grid voltage, which is considered as the phase reference. This assumption allows working with a moderate mathematical complexity in the analysis. As a consequence of the voltage regulation loop, the oscillatory component of the DC voltage appears in the current amplitude $i_{max}(t)$ with an average value of I_{max} and a harmonic of amplitude I_2 and phase ϕ which will depend on the frequency response of the loop compensator. Then, $i_{max}(t)$ is expressed as

$$i_{max}(t) = I_{max} + I_2\, sin(2\omega t + \phi) \tag{44}$$

The sliding surface is defined by $S(x) = i_g - i_L$. At the surface, the invariance condition is fulfilled if $S(x) = 0$ *and* $\dot{S}(x) = 0$. The derivative of the current reference is given by

$$\frac{di_{max}}{dt} = \frac{dI_{max}}{dt} + 2I_2\omega\cos(2\omega t + \phi) + I_2\frac{d\phi}{dt}\cos(2\omega t + \phi) + \frac{dI_2}{dt}sin(2\omega t + \phi) \quad (45)$$

Then, we have

$$\frac{dS}{dt} = \frac{di_g}{dt} - \frac{di_L}{dt} = \frac{di_{max}}{dt}sin\,\omega t + \omega i_{max}\cos\omega t + \frac{v_g}{L} - u\frac{v_C}{L} \quad (46)$$

Since $\left.\frac{dS}{dt}\right|_{u=u_{eq}} = 0$, it can be derived

$$u_{eq} = \frac{1}{v_C}\left(L\frac{di_{max}}{dt}sin\,\omega t + L\omega i_{max}\,cos\,\omega t + V_{max}\,sin\,\omega t\right) \quad (47)$$

Replacing in the equation describing the motion of v_C, we obtain

$$C\frac{dv_C}{dt} = \frac{P}{v_C} - \frac{1}{v_C}i_{max}\,sin\,\omega t\left(L\frac{di_{max}}{dt}sin\,\omega t + L\omega i_{max}\,cos\,\omega t + V_{max}\,sin\,\omega t\right) \quad (48)$$

Then,

$$\begin{aligned} Cv_C\frac{dv_C}{dt} = P &- \frac{V_{max}i_{max}}{2} - \frac{Li_{max}}{2}\frac{di_{max}}{dt} - \frac{L\omega {i_{max}}^2}{2}\sin 2\omega t + \frac{Li_{max}}{2}\frac{di_{max}}{dt}\cos 2\omega t \\ &+ \frac{V_{max}i_{max}}{2}\cos 2\omega t \end{aligned} \quad (49)$$

Considering (42) and (44), after some tedious calculations, it is obtained the equilibrium point of (49) (derivatives equal to zero)

$$\begin{aligned} P = \frac{V_{max}I_{max}}{2} &- \frac{V_{max}I_2}{4}\sin\phi + \frac{V_{max}I_2}{2}sin(2\omega t + \phi) - \frac{L{I_2}^2\omega}{8}\sin(2\omega t + 2\phi) \\ &+ LI_{max}I_2\omega\cos(2\omega t + \phi) + \frac{L\omega {I_{max}}^2}{2}sin\,2\omega t + \frac{L{I_2}^2\omega}{4}sin\,2\omega t \\ &- \frac{V_{max}I_{max}}{2}\cos 2\omega t - \frac{V_{max}I_2}{4}\sin(4\omega t + \phi) \\ &- LI_{max}I_2\omega\cos(4\omega t + \phi) + \frac{L{I_2}^2\omega}{2}\sin(4\omega t + 2\phi) \\ &- \frac{L{I_2}^2\omega}{4}\sin(6\omega t + 2\phi) - \frac{L\omega {I_2}^2}{8}\sin(6\omega t + 2\phi) \end{aligned} \quad (50)$$

By averaging the previous expression over a period of π, the average power is obtained as

$$< P >= \frac{V_{max}I_{max}}{2} - \frac{V_{max}I_2}{4}\sin\phi \quad (51)$$

Then, since< P >= $\overline{P}$, then:

$$\bar{P} = \frac{V_{max}}{2}\left(I_{max} - \frac{I_2}{2}\sin\phi\right) \tag{52}$$

On the other hand, from (42) and (44) after some simple manipulations, we have

$$i_g(t) = [I_{max} + I_2\, sin(2\omega t + \phi)]\, sin(\omega t) \tag{53}$$

$$i_g(t) = \left(\frac{1}{2}\sqrt{4{I_{max}}^2 - 4I_{max}I_2\sin\phi + {I_2}^2}\right) sin(\omega t + \varphi) - \frac{I_2}{2} cos(3\omega t + \phi) \tag{54}$$

where

$$\varphi = \text{atan}\left(\frac{I_2\cos\phi}{2I_{max} - I_2\sin\phi}\right) \tag{55}$$

The power on the AC side is computed as $p_g(t) = v_g(t)i_g(t)$

$$\begin{aligned} p_g(t) = V_{max}\Bigg[&\left(\sqrt{{I_{max}}^2 - I_{max}I_2\sin\phi + \frac{{I_2}^2}{4}}\right) sin(\omega t + \varphi) \\ &- \frac{I_2}{2} cos(3\omega t + \phi)\Bigg] sin\,\omega t \end{aligned} \tag{56}$$

$$\begin{aligned} p_g(t) = \frac{V_{max}}{2}&\left(\sqrt{{I_{max}}^2 - I_{max}I_2\sin\phi + \frac{{I_2}^2}{4}}\right)(\cos\varphi - \cos(2\omega t + \alpha)) \\ &- \frac{V_{max}I_2}{2}[\sin(4\omega t + \phi) - \sin(2\omega t + \phi)] \end{aligned} \tag{57}$$

The mean value of the power is obtained as

$$|\overline{p_g}| = \frac{V_{max}}{2}\left(\sqrt{{I_{max}}^2 - I_{max}I_2\sin\phi + \frac{{I_2}^2}{4}}\right)\cos\left[\text{atan}\left(\frac{I_2\cos\phi}{2I_{max} - I_2\sin\phi}\right)\right] \tag{58}$$

Since $\cos\left[\text{atan}\left(\frac{I_2\cos\phi}{2I_{max} - I_2\sin\phi}\right)\right] = \frac{1}{\sqrt{1+x^2}}$, we obtain

$$\overline{p_g} = \frac{V_{max}}{2}\left(I_{max} - \frac{I_2}{2}sin\,\phi\right) \tag{59}$$

which confirms (52) for the mean power on the DC side. From (43), we have

$$\frac{dv_C}{dt} = \frac{dV_{dc}}{dt} + 2\omega V_2\cos(2\omega t + \gamma) + V_2\cos(2\omega t + \gamma)\frac{d\gamma}{dt} + \frac{dV_2}{dt}\sin(2\omega t + \gamma) \tag{60}$$

and then,

$$
\begin{aligned}
Cv_C\frac{dv_C}{dt} = C\Big[&V_{dc}\frac{dV_{dc}}{dt} + V_2\frac{dV_{dc}}{dt}\sin(2\omega t+\gamma) + 2V_{dc}V_2\omega\, cos(2\omega t+\gamma)\\
&+ V_{dc}V_2\frac{d\gamma}{dt}\cos(2\omega t+\gamma) + V_{dc}\frac{dV_2}{dt}sin(2\omega t+\gamma)\\
&+ {V_2}^2\omega\, sin(4\omega t+2\gamma) + 2{V_2}^2\frac{d\gamma}{dt}\sin(4\omega t+2\gamma) + \frac{V_2}{2}\frac{dV_2}{dt}\\
&- V_2\frac{dV_2}{dt}\cos(4\omega t+2\gamma)\Big]
\end{aligned}
\tag{61}
$$

By equalizing (50) and (61) evaluated at the equilibrium point (derivatives equal to zero) and keeping only the double frequency components, we have

$$
\begin{aligned}
&2CV_{dc}V_2\omega\, cos(2\omega t+\gamma)\\
&\quad= -\frac{V_{max}I_2}{2}sin(2\omega t+\phi) + \frac{L{I_2}^2\omega}{8}\sin(2\omega t+2\phi)\\
&\quad- LI_{max}I_2\omega\cos(2\omega t+\phi) - \frac{L\omega{I_{max}}^2}{2}sin\,2\omega t - \frac{L{I_2}^2\omega}{4}sin\,2\omega t\\
&\quad+ \frac{V_{max}I_{max}}{2}\cos 2\omega t
\end{aligned}
\tag{62}
$$

from which, after some tedious calculations, we obtain

$$
V_2 = \frac{\sqrt{\begin{aligned}&\Big[\omega L\left(4{I_{max}}^2 + {I_2}^2(2-\cos 2\phi)\right) + 4V_{max}I_2\cos\phi - 8LI_{max}I_2\omega\sin\phi\Big]^2\\ &+\left(\omega L{I_2}^2\sin 2\phi + 4V_{max}I_{max} - 4\omega LI_{max}I_2\cos\phi - 8V_{max}I_2\sin\phi\right)^2\end{aligned}}}{16CV_{dc}\omega}
\tag{63}
$$

and:

$$
\gamma = \operatorname{atan}\left(\frac{\omega L\left(4{I_{max}}^2 + {I_2}^2(2-\cos 2\phi)\right) + 4V_{max}I_2\cos\phi - 8LI_{max}I_2\omega\sin\phi}{\omega L{I_2}^2\sin 2\phi + 4V_{max}I_{max} - 4\omega LI_{max}I_2 - 8V_{max}I_2\sin\phi}\right)
\tag{64}
$$

Considering the ideal case with $I_2 = 0$, and $\phi = 0$, then, we have

$$
V_2 = \frac{I_{max}}{4CV_{dc}\omega}\sqrt{\omega^2L^2{I_{max}}^2 + {V_{max}}^2}
\tag{65}
$$

and

$$
\gamma = \operatorname{atan}\left(\frac{\omega LI_{max}}{V_{max}}\right)
\tag{66}
$$

Therefore, the parameters which define the DC-link voltage ripple waveform have been determined. Figure 10 shows simulation results of the ripple voltage obtained in PSIM for different sets of parameters validating the above theoretical predictions.

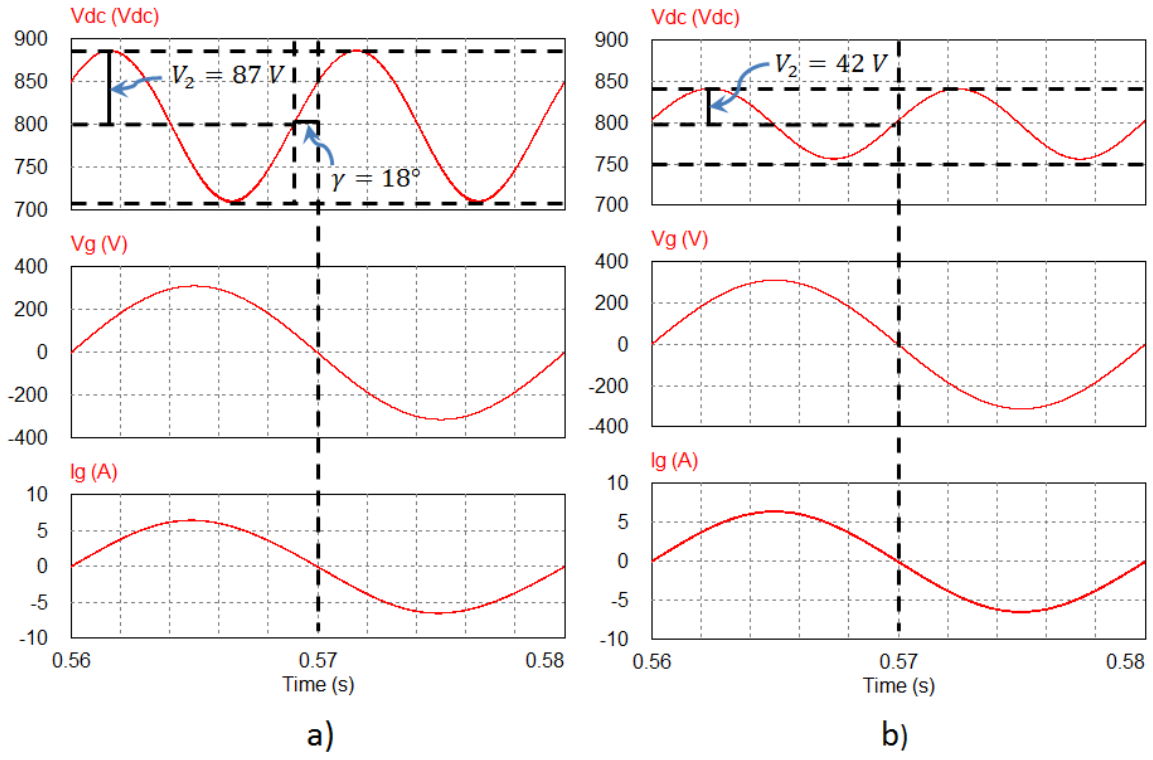

Figure 10. Validation of the predicted parameters of the ripple in the voltage of the DC bus: a) case 1 (L = 100 mH, C = 27 µF); b) case 2 (L = 10mH, C = 47 µF).

In both cases of figure 10 a regulated DC bus voltage of 800 V and an input power of 1 kW have been used. The levels of voltage and power have been selected in order to better illustrate the studied behavior in the voltage ripple. A grid source of 220 V at 50 Hz is used. Differences between the amplitude and phase displacement of the voltage ripple are observed for two set of values of the passive parameters (L and C). The differences between the simulated values and the theoretically computed values of the amplitude and phase displacement of the voltage ripple are lower than 0.5%. It is worth to note that the phase displacement appears for higher values of inductance; however, for an equal value of power the effect is negligible when the inductance has a value ten times lower. Then, the amplitude of the voltage ripple can be imposed by means of the passive elements. The inductor constrains the derivative of the output current and hence is designed for a maximum current value and a hysteresis size, so that, the parameter which defines the voltage ripple is the bus capacitor.

6.2. Total Harmonic Distortion of the output current

The presence of the component I_2 is a consequence of the ripple in the voltage of the DC bus and its propagation through the outer control loop. To quantify this aspect, the frequency response of the controller must be analyzed. We have

$$C(s) = \frac{I_{max}(s)}{E(s)} = \frac{I_{max}(s)}{V_{ref}(s) - V_c(s)} = -\frac{K_c(T_c s + 1)}{s(T_f s + 1)} \tag{67}$$

The gain and phase of the controller as a function of the frequency are

$$K_{v_c i_m} = |C(\omega)| = \frac{K_c}{\omega}\sqrt{\frac{1 + {T_c}^2\omega^2}{1 + {T_f}^2\omega^2}} \tag{68}$$

$$\beta(\omega) = -270° + \text{atan}\left(\frac{1 + T_C T_f \omega^2}{\omega(T_f - T_C)}\right) \tag{69}$$

Then, with $\omega = 2\pi f$ and $f = 2f_{grid}$, the amplitude and phase of the component I_2 is given by

$$I_2 = \frac{K_c V_2}{4\pi f_{grid}}\sqrt{\frac{1 + 16\pi^2 {T_c}^2 {f_{grid}}^2}{1 + 16\pi^2 {T_f}^2 {f_{grid}}^2}} \tag{70}$$

and:

$$\phi = \gamma - \text{atan}\left(\frac{1 + 16\pi^2 T_C T_f {f_{grid}}^2}{4\pi f_{grid}(T_f - T_C)}\right) \tag{71}$$

The validation of the above expression is graphically presented in figure 11. A reference of 400 V is used to the voltage regulation loop. The inverter is connected to a 220 V at 50 Hz grid injecting a power of 100 W.

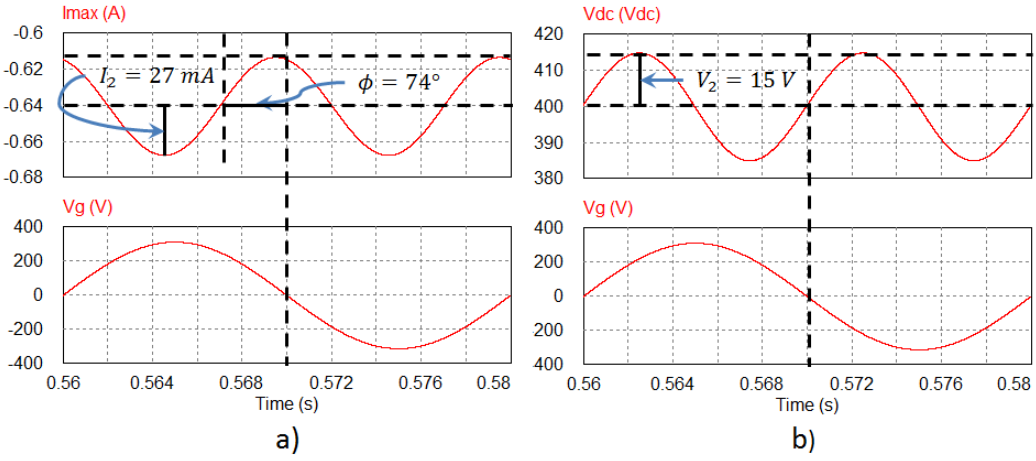

Figure 11. Validation of the predicted parameters of the current amplitude i_{max} (L = 10mH, C = 47 µF).

The transfer function of the voltage controller is defined as follows

$$C(s) = -\frac{0.1(0.06s + 1)}{s(0.005s + 1)} \tag{72}$$

The 100 Hz component of the ripple is attenuated for the controller with a gain of -54.7 dB. Further, a phase lead of 74° is observed between the AC components of the voltage and the current reference. Considering that the PLL gives a perfect sinusoidal waveform with normalized amplitude, the harmonic content of the current can be only introduced through the amplitude signal i_{max}. The current i_g in expression (54) can be rewritten as

$$i_g = \underbrace{\frac{1}{2}\sqrt{4{I_{max}}^2 - 4I_{max}I_2 \sin\phi + {I_2}^2}}_{I_{g1}} sin(\omega t + \varphi) - \underbrace{\frac{I_2}{2}}_{I_{g3}} \cos(3\omega t + \phi) \tag{73}$$

where $i_{g1} = I_{g1}\, sin(\omega t + \varphi)$ and $i_{g3} = I_{g3} \cos(3\omega t + \phi)$. Then, we have:

$$i_g = i_{g1} + i_{g3} = I_{g1}\, sin(\omega t + \varphi) - I_{g3} \cos(3\omega t + \phi) \tag{74}$$

However, the ripple content of the current has a non-negligible effect in the THD and hence must be also considered. Although the frequency varies in the ripple waveform, because of its triangular shape, the RMS value of the ripple can be approximated as $i_{rip} = \Delta/\sqrt{3}$. Then, it is possible to obtain the RMS values of the current components and then to compute the total harmonic distortion given by

$$THD - F \cong \frac{\sqrt{RMS(i_{g3})^2 + {i_{rip}}^2}}{RMS(i_{g1})} = \sqrt{\frac{3{I_2}^2 + 8\Delta^2}{6(4{I_{max}}^2 - 4I_{max}I_2 \sin\phi + {I_2}^2)}} \tag{75}$$

As it can be shown in figure 12, different THD values can be obtained for a same value of amplitude in the voltage ripple. The figure 12a shows the effect of the voltage ripple when a value of 0.00005 seconds is settled in the filter time constant of the controller (T_f). This value corresponds to a poor filtering at 100 Hz. Figure 12b shows the result using a value of 0.005 for T_f , which is the selected value in the design procedure. The action of the filter is too relevant because the harmonic distortion reduces from a 7.98% to a 4.45%.

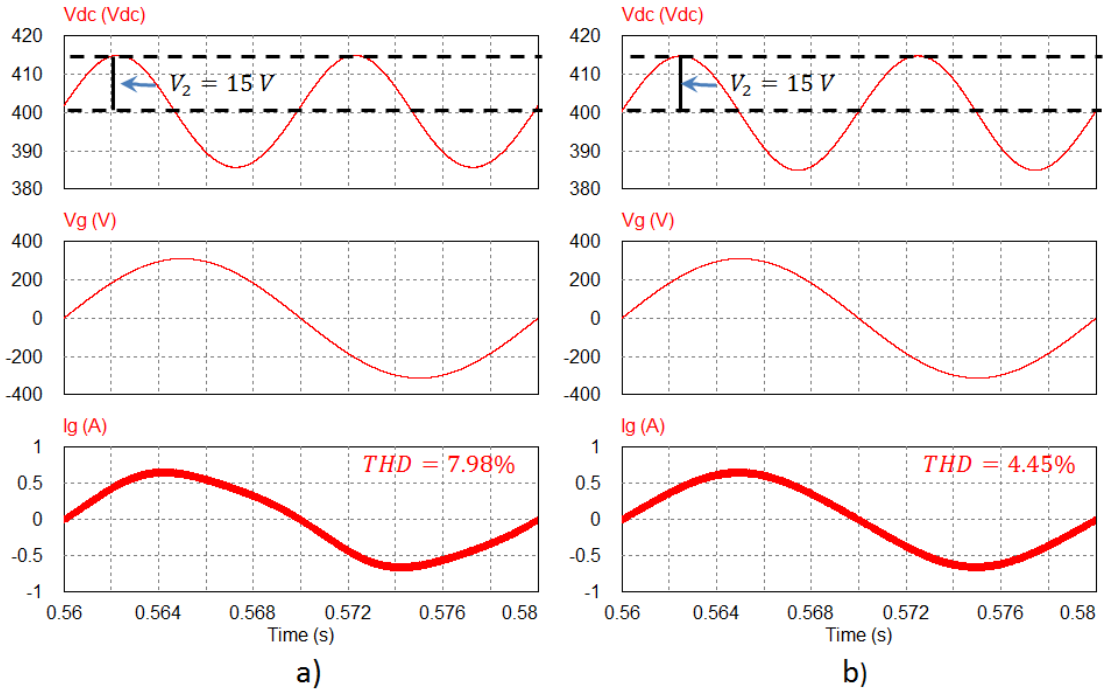

Figure 12. Effect of the ripple in the current THD (L = 10 mH, C = 27 µF): a) case 1 (T_f = 0.00005); b) case 2 (T_f = 0.005).

It is worth to note that the effect of the ripple component of the current is significant. Considering an ideal sliding motion in the current ($\Delta = 0$), the THD reduces to 7.01% and 2.17% for the cases in figure 12 respectively.

6.3. Power factor and displacement power factor

The power factor is a key aspect of the grid connected systems. Because of the presence of some harmonic content, it is possible to differentiate the effect of the current phase shift using the Displacement Power Factor (DPF) or to have combined the effect of the current displacement and the harmonic content in the Power Factor (PF). From (57), we have

$$\varphi = \operatorname{atan}\left(\frac{\frac{I_2}{2}\cos\phi}{I_{max} - \frac{I_2}{2}\sin\phi}\right)$$

Hence, the displacement power factor is obtained as

$$DPF = \cos\varphi = \cos\left[\operatorname{atan}\left(\frac{\frac{I_2}{2}\cos\phi}{I_{max} - \frac{I_2}{2}\sin\phi}\right)\right] = \frac{2I_{max} - I_2\sin\phi}{\sqrt{4{I_{max}}^2 - 4I_{max}I_2\sin\phi + {I_2}^2}} \tag{76}$$

On the other hand, from (74), we have that $i_g = I_{g1}\,sin(\omega t + \varphi) - I_{g3}\cos(3\omega t + \phi)$, where the RMS value of the grid current i_g can be obtained from the RMS values of its frequency components as

$$RMS(i_g) = I_g = \sqrt{\frac{{I_{g1}}^2}{2} + \frac{{I_{g3}}^2}{2} + \frac{\Delta^2}{3}} = \sqrt{\frac{6{I_{max}}^2 - 6I_{max}I_2\sin\phi + 3{I_2}^2 + 4\Delta^2}{12}} \tag{77}$$

From (55), we have

$$RMS(i_{g1}) = I_{g1} = \sqrt{\frac{4{I_{max}}^2 - 4I_{max}I_2\sin\phi + {I_2}^2}{8}} \tag{78}$$

Then, the power factor can be obtained from

$$PF = \frac{P_g}{S_g} = \frac{RMS(v_g)RMS(i_{g1})\cos\varphi}{RMS(v_g)RMS(i_g)} = \frac{I_{g1}}{I_g}\cos\varphi = \frac{I_{g1}}{I_g}DPF$$

Therefore

$$PF = \left[\sqrt{\frac{12{I_{max}}^2 - 12I_{max}I_2\sin\phi + 3{I_2}^2}{12{I_{max}}^2 - 12I_{max}I_2\sin\phi + 6{I_2}^2 + 8\Delta^2}}\right]DPF \tag{79}$$

Note that a reduced current component I_2 directly increases the power factor; also, observe the effect of the angle ϕ in the power factor. As an illustrative example, the DPF and the PF have been computed for the same parameters used in the simulated results in subsection 6.2. For the first case (THD=7.98%) which corresponds to the worst THD, the values of DPF and PF are 0.997 and 0.994 respectively. For the second case

(THD=4.45%) which corresponds to the best THD, the values of DPF and PF are 1.000 and 0.999 respectively.

7. Experimental results

In order to experimentally validate the theoretical analyses, the controller design and the simulation results, a 100 W prototype has been implemented. The experiments uses a boost DC-DC stage operating as a power source which is fed by a low voltage source. The change in the input power of the inverter is induced using the control of the DC-DC stage.

7.1 Prototype and experimental set-up

A 100 W prototype of the grid connected inverter has been implemented to work with a regulated input voltage of 400 VDC and a grid voltage of 220 V at 50 Hz. The power section of the prototype is composed by an inductor of 10 mH, two paralleled capacitors of 11 µF and four MOSFET IPR60R099C6 with CoolMOS Technology and low ESR (99mΩ) using a RCD snubber per MOSFET with a fast switching diode PR1007G, a thin film capacitor of 4.7 nF - 1600 V and a resistance of 470 kΩ - 1W. A pair of integrated circuits IR2110 was used to drive the power MOSFETs. The inductor current is measured using an effect Hall current sensor CAS 6 from LEM. The control section is implemented using a microcontroller dsPIC30F4011 and some classical discrete electronic circuits. The current reference is generated inside the microcontroller synchronized with the grid through an external PLL. The current controller is digitally implemented whereas the voltage controller is implemented with analog electronics. The set-up for measurements shown in figure 13 consists of the oscilloscope MSO3014, the current probes TCP202 and TCPA300, and the high voltage differential probe P5210 from Tektronix, the power supplies Rohde & Schwartz NGSM 32/10 and Multimeteix XA3033, and the multimeter HP34401A from Hewlett Packard.

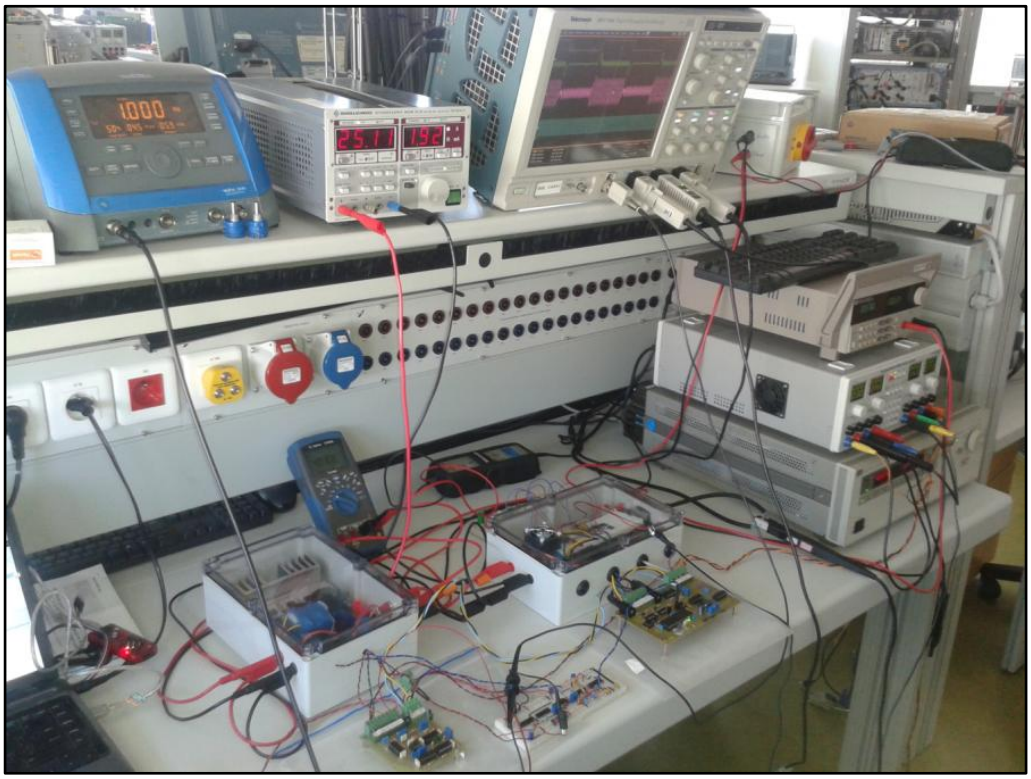

Figure 13. Experimental set-up and inverter prototype.

7.1. Current signal generation and current controller

The current reference is generated using a pre-sampled sine-waveform stored in a table in the memory of the microcontroller, which has 1024 samples per grid period. An external zero crossing detector generate a square-wave signal at the grid frequency. A discrete PLL based on the integrated circuits CD4046 and CD4060 is synchronized with this signal generating a high frequency signal (HF: four times the sampling frequency) and a low frequency signal (LF: grid frequency) with a phase lag of 90°. The algorithm of the microcontroller uses the LF signal to start the counter of the table while the HF signal increases the pointer of the table once every four cycles drawing the synchronized reference. The current controller is also implemented in the microcontroller constraining the switching frequency using the HF signal. Figure 14 shows the grid voltage compared with the current reference, together with the gate signals of the H-bridge (figure 14a) or the low frequency signal LF (figure 14b). As it can be observed, the flattening of the grid voltage has no influence in the grid current showing the advantages of the PLL.

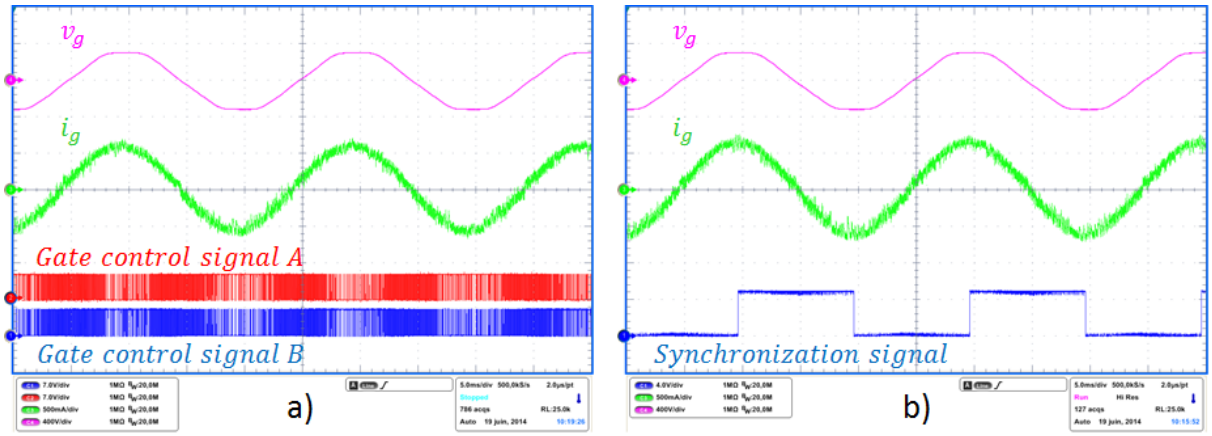

Figure 14. a) grid voltage, output current and control signals (gate signals); b) grid voltage, output current and synchronization signal (90° of phase displacement).

7.1. Voltage regulation of the DC-Link

In order to assess the dynamic response of the regulated DC bus, a power perturbation has been inserted using the DC-DC converter operating as a SM-LFR (Cid-Pastor, Martinez-Salamero, El Aroudi, Giral, Calvente & Leyva 2013). The conductance value of the control is changed introducing a square-wave signal as shown in figure 15. In figure 15a it is depicted the case of a change from 50 to 80 W and vice versa with a frequency of 1 Hz. In figure 15b, the power levels of the changes are modified for 100 and 20 W.

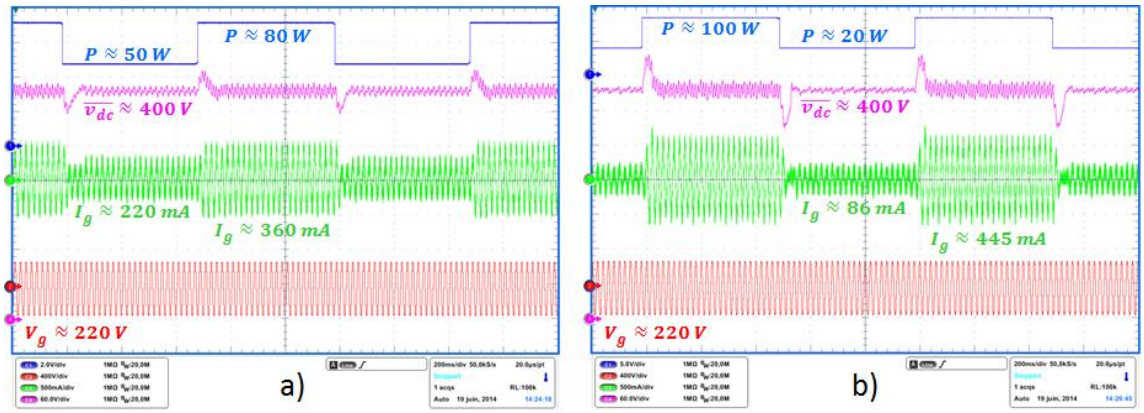

Figure 15. Transient response of the DC voltage loop: a) 50 W - 80 W – 50 W; b) 20 W – 100 W – 20 W.

7.2. Effect of the low pass filter on the current distortion

The effect of the filtering time- constant T_f of the controller in the harmonic distortion of the output current is depicted in the oscilloscope waveforms of figure 16. As it is shown for the same amplitude of the ripple in the DC bus, the current waveform is cleaner when the parameter T_f is close to the optimum value (4% in the figure 16b). Also, it is possible to observe that the amplitude of the current reference i_{max} has a more notorious distortion when the current signal has higher THD (7.3% in figure 16a). This result confirms the expected reduction of the effect of the voltage ripple in the current THD.

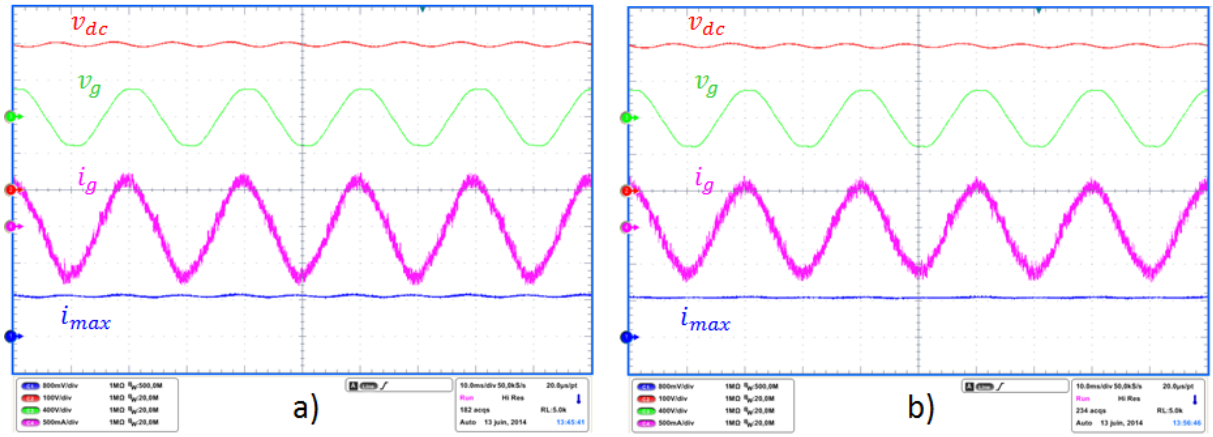

Figure 16. Experimental results showing the filter effect a) $T_f = 0.0005$; b) $T_f = 0.005$.

8. Conclusions

The concept of a sliding mode controlled Power Source Inverter (PSI) and the theoretical expressions describing its dynamic performance and power quality when it is connected to the ac grid have been presented. The converter operating in bipolar and unipolar commutation modes is controlled using a nonlinear control based on a first order sliding mode control law tracking a pure sine current reference whose amplitude is given by a linear controller regulating the voltage of the DC-link of the microinverter. The model of the ideal sliding dynamics is used to design the voltage regulation loop and also to assess the resulting THD on the output current with the aim of eventually reducing it to admissible levels. The power factor, the displacement power factor and the total harmonic distortion are analyzed by means of the harmonic balance of the converter. Simulations results have illustrated the theory and have been complemented by means of experimental results, which have shown the potentialities of the proposed PSI as the output stage of a dual stage microinverter.

References

Amirahmadi A., Chen L., Somani U., Hu H., Kutkut N. & Bartarseh I. (2014, June) High Efficiency Dual-Mode Current Modulation Method for Low-Power DC/AC Inverters. *IEEE Transactions on Power Electronics,* 29 (6), 2638-2642.

Baker D.M., Agelidis V.G. & Nayer C.V. (1997, July). A comparison of tri-level and bi-level current controlled grid-connected single-phase full-bridge inverters. In the *IEEE International Symposium on Industrial Electronics (ISIE),* 463-468.

Beser E., Arifoglu B., Camur S. & Beser E.K. (2010, December) A grid-connected photovoltaic power conversion system with single-phase multilevel inverter. *Solar Energy*, *84*, 2056-2067.

Blaabjerg F., Chen Z. & Kjaer S.B. (2004, September). Power electronics as efficient interface in dispersed power generation systems. *IEEE Transactions on Power Electronics*, *19 (5),* 1184-1194.

Calais M., Agelidis V.G. & Dymond M.S. (2011, January). A cascaded inverter for transformer-less single-phase grid-connected photovoltaic systems. *Renewable Energy, 22,* 255-262.

Calais M., Myrzik J., Spoone T. & Agelidis V. G. (2005, September). Inverters for Single-phase Grid Connected Photovoltaic Systems - An Overview. IEEE Transactions on Industrial Applications, *41 (5),* 1292-1306.

Carrasco J.M., Franquelo L.G., Bialasiewicz J.T., Galvan E., Guisado R.C.P., …Prats Ma.A.M. (2006, June). Power-Electronic Systems for the Grid Integration of Renewable Energy Sources: A Survey. *IEEE Transactions on Industrial Electronics, 53 (4),* 1002-1016.

Cid-Pastor A., Martinez-Salamero L., El Aroudi A., Giral R., Calvente J. & Leyva R. (2013, May) Synthesis of loss-free-resistors based on sliding-mode control and its applications in power processing. Control Engineering Practice, 21 (5), 689-699.

Cruz Martins D. & Demonti R. (2002, May). Grid Connected PV System Using Two Energy Processing Stages. In the *Conference Record of the 29th IEEE Photovoltaic Specialists Conference*, 1649-1652.

Dai X. & Chao Q. (2009, April). The Research of Photovoltaic Grid-Connected Inverter Based on Adaptive Current Hysteresis Band Control Scheme. In the *International Conference on Sustainable Power Generation and Supply (SUPERGEN)*. 1-8.

Edwin F.F., Weidong X. & Khadkikar V. (2014, November). Dynamic Modeling and Control of Interleaved Flyback Module-Integrated Converter for PV Power Applications. *IEEE Transactions on Industrial Electronics, 61 (3),* 1377-1388.

Eltawil M. A. & Zhao Z. (2010). Grid-Connected Photovoltaic Power Systems: Technical and Potential Problems—A review," *Renewable and Sustainable Energy Reviews, 14*, 112-129.

Fernao Pires V., Sousa D.M. & Martins J.F. (2014, June). Controlling a grid-connected T-type three level inverter system using a sliding mode approach. In the *IEEE International Symposium on Industrial Electronics,* 2002-2007.

Gao M., Chen M., Zhang C. & Qian Z. (2014, July). Analysis and Implementation of an Improved Flyback Inverter for Photovoltaic AC Module Applications. *IEEE Transactions on Power Electronics, 29 (7),* 3428-3444.

Ho C.N.M., Cheung V.S.P. & Chung H.S. (2009, November). Constant-Frequency Hysteresis Current Control of Grid-Connected VSI Without Bandwidth Control. *IEEE Transactions on Power Electronics, 24 (11)*, 2484-2495, Nov. 2009.

IEC Standard. (1995). Electromagnetic Compatibility (EMC) Part 3-2: Limits-Limits for Harmonic Current Emissions (Equipment Input Current Under 16 A per Phase). EN 61000-3-2.

IEC Standard. (2002). Characteristics of the utility interface for photovoltaic (PV) systems. IEC 61727.

IEEE Standard. (2000). IEEE Recommended Practice for Utility Interface of Photovoltaic (PV) Systems. IEEE 929-2000.

IEEE Standard. (2005). IEEE Standard Conformance Test Procedures for Equipment Interconnecting Distributed Resources with Electric Power Systems. IEEE 1547.1-2005.

Jiabing H., Zhu Z.Q., Nian H., Shang L. & He Y. (2010, September). Sliding mode current control of grid-connected voltage source converter. In the *IEEE Energy Conversion Congress and Exposition (ECCE),* 912-919.

Jiang S., Cao D., Li Y. & Peng F.Z. (2012, November). Grid-Connected Boost-Half-Bridge Photovoltaic Microinverter System Using Repetitive Current Control and Maximum Power Point Tracking. *IEEE Transactions on Power Electronics*, 27 (11), 4711-4722.

Karimi-Ghartemani M., Khajehoddin S.A., Jain P. & Bakhshai A. (2013, July). A Systematic Approach to DC-Bus Control Design in Single-Phase Grid-Connected Renewable Converters. *IEEE Transactions on Power Electronics, 28 (7),* 3158-3166.

Kerekes T., Teodorescu R., Rodriguez P., Vazquez G. & Aldabas E. (2011, January). A New High-Efficiency Single-Phase Transformerless PV Inverter Topology. *IEEE Transactions on Industrial Electronics, 58 (1)* 184-191.

Kim I.-S. (2006, October). Sliding mode controller for the single-phase grid-connected photovoltaic system. *Applied Energy*, *83*, 1101-1115.

Kim Y.-H., Shin S-C., Lee J-H., Jung Y-C., & Won C-Y. (2014, February). Soft-Switching Current-Fed Push–Pull Converter for 250-W AC Module Applications. *IEEE Transactions on Power Electronics, 29 (2)*, 863-872.

Kim Y.-H, Jang J., Shin S. & Won C. (2014, December). Weighted-Efficiency Enhancement Control for a Photovoltaic AC Module Interleaved Flyback Inverter Using a Synchronous Rectifier. *IEEE Transactions on Power Electronics, 29 (12)* 6481-6493.

Kjaer S.B., Pedersen J.K. & Blaabjerg F. (2005, September). A Review of Single-Phase Grid-Connected Inverters for Photovoltaic Modules. *IEEE Transactions on Industry Applications*, *41 (5),* 1292-1306.

Kjaer S.B., Pedersen J.K. & Blaabjerg F. (2012, October). Power Inverter Topologies for Photovoltaic Modules – A Review. In *the 37th IAS Annual Meeting, Conference Record of the Industry Applications Conference*, *2,* 782-788.

Kojabadi H.M., Yu B., Gadoura I. A., Chang L. & Ghribi M. (2006, July). A Novel DSP-Based Current-Controlled PWM Strategy for Single Phase Grid Connected Inverters. *IEEE Transactions on Power Electronics, 21 (4),* 985-993.

Krismadinata, Rahim N.A. & Selvaraj J. (2007, November). Implementation of Hysteresis Current Control for Single-Phase Grid Connected Inverter. In the *7th International Conference on Power Electronics and Drive Systems (PEDS)*, 1097-1101.

Li Q. & Wolfs P. (2008, May). A Review of the Single Phase Photovoltaic Module Integrated Converter Topologies with Three Different DC Link Configurations. *IEEE Transactions on Power Electronics, 23 (3),* 1320-1333.

Meneses D., Blaabjerg F., García O. & Cobos J.A. (2013, June). Review and Comparison of Step-Up Transformerless Topologies for Photovoltaic AC-Module Application. *IEEE Transactions on Power Electronics, 28 (6),* 2649-2663.

National Semiconductors. (2011). Application Note 2116. SolarMagic ICs in Micro-Inverter Applications, Literature Number: SNVA471A.

Negroni J.J., Meza C., Biel D. & Guinjoan F. (2005, June). Control of a buck inverter for grid-connected PV systems: a digital and sliding mode control approach. In the *IEEE International Symposium on Industrial Electronics, 2,* 739-744.

Philipson L. (2010). Distributed and dispersed generation: addressing the spectrum of consumer needs. In the *IEEE Power Engineering Society Summer Meeting*, *3*, 1663-1665.

Rashid M. (2001). *Power Electronics Handbook*. London: Academic Press.

Rodriguez C. & Amaratunga G.AJ. (2006, January). Dynamic maximum power injection control of AC photovoltaic modules using current-mode control. *IEE Proceedings Electric Power Applications, 153 (1)*, 83-87.

Schimpf F. & Norum L. E. (2008, June). Grid connected Converters for Photovoltaic, State of the Art, Ideas for Improvement of Transformerless Inverters. *In the Nordic Workshop on Power and Industrial Electronics*.

Sher H.A. & Addoweesh K.E. (2012, December). Micro-inverters - Promising Solutions in Solar Photovoltaics. *Energy for Sustainable Development*, *16,* 389-400.

Singer S. (1990, January) Realization of loss-free resistive elements. *IEEE Transactions on Circuits and Systems, 37 (1),* 54-60.

Sira-Ramirez H. & Silva-Ortigoza R. *Control Design Techniques in Power Electronic Devices* (1th ed.). Germany: Springer, 2006.

Sukesh N., Pahlevaninezhad M. & Jain P.K. (2014, April). Analysis and Implementation of a Single-Stage Flyback PV Microinverter with Soft Switching. *IEEE Transactions on Industrial Electronics, 61 (4),* 1819-1833.

UL Standard. (2010). Standard for Safety Inverters, Converters, Controllers and Interconnection System Equipment for Use with Distributed Energy Resources. UL 1741.

Utkin V., Guldner J. & Shi J. (2009). *Sliding mode control in electromechanical* systems (4th ed.). London: CRC Press, Taylor and Francis Group.

Vasconcelos Araújo S., Zacharias P. & Mallwitz R. (2010, September). Highly Efficient Single-Phase Transformerless Inverters for Grid-Connected Photovoltaic Systems. *IEEE Transactions on Industrial Electronics, 57 (9),* 3118-3128.

Xiao H., Xie S., Chen Y., & Huang R. (2011, May). An Optimized Transformerless Photovoltaic Grid-Connected Inverter. *IEEE Transactions on Industrial Electronics, 58 (5)*, 1887-1895.

Xue Y., Chang L., Kjaer S.B., Bordonau J. & Shimizu T. (2004, September). Topologies of single-phase inverters for small distributed power generators: an overview. *IEEE Transactions on Power Electronics, 19 (5)* 1305-1314.

Yu W., Lai J-S., Qian H. & Hutchens C. (2011, April). High-Efficiency MOSFET Inverter with H6-Type Configuration for Photovoltaic Nonisolated AC-Module Applications. *IEEE Transactions on Power Electronics, 26 (4)*, 1253-1260.

Zhang L., Sun K., Xing Y., Feng L. & Ge H. (2011, February). A Modular Grid-Connected Photovoltaic Generation System Based on DC bus. *IEEE Transactions on Power Electronics, 26 (2)*, 523-531.

Zhang Z. He X.-F. & Liu Y.-F. (2013, November). An Optimal Control Method for Photovoltaic Grid-Tied-Interleaved Flyback Microinverters to Achieve High Efficiency in Wide Load Range. *IEEE Transactions on Power Electronics, 28 (11),* 5074-5087.

Zhou Y., Liu L. & Li H. (2013, June). A High-Performance Photovoltaic Module-Integrated Converter (MIC) Based on Cascaded Quasi-Z-Source Inverters (qZSI) Using eGaN FETs. *IEEE Transactions on Power Electronics, 28 (6),* 2727-2738.